Detailed study of the ELAIS N1 field with the uGMRT – I. Characterizing the 325 MHz foreground for redshifted 21 cm observations

Arnab Chakraborty,[1] Abhirup Datta,[1] Samir Choudhuri,[2] Nirupam Roy,[3] Huib Intema [4] Madhurima Choudhury [1] Kanan K. Datta,[5] Srijita Pal,[6] Somnath Bharadwaj,[6] Prasun Dutta [7] and Tirthankar Roy Choudhury [2]

[1] *Discipline of Astronomy, Astrophysics and Space Engineering, Indian Institute of Technology Indore, Indore 453552, India*
[2] *National Centre for Radio Astrophysics, Post bag 3, Ganeshkhind, Pune 411007, India*
[3] *Department of Physics, Indian Institute of Science, Bangalore 560012, India*
[4] *Leiden Observatory, Leiden University, Niels Bohwerg 2, NL-2333CA Leiden, the Netherlands*
[5] *Department of Physics, Presidency University, 86/1 College Street, Kolkata 700073, India*
[6] *Department of Physics & Centre for Theoretical Studies, IIT Kharagpur, Kharagpur 721302, India*
[7] *Department of Physics, IIT (BHU), Varanasi 221005, India*

ABSTRACT

In this first paper of the series, we present initial results of newly upgraded Giant Metrewave Radio Telescope (uGMRT) observation of European Large-Area ISO Survey-North 1 (ELAIS-N1) at 325 MHz with 32 MHz bandwidth. Precise measurement of fluctuations in Galactic and extragalactic foreground emission as a function of frequency as well as angular scale is necessary for detecting redshifted 21 cm signal of neutral hydrogen from Cosmic Dawn, epoch of reionization (EoR) and post-reionization epoch. Here, for the first time we have statistically quantified the Galactic and extragalactic foreground sources in the ELAIS-N1 field in the form of angular power spectrum using the newly developed tapered gridded estimator (TGE). We have calibrated the data with and without direction-dependent calibration techniques. We have demonstrated the effectiveness of TGE against the direction-dependent effects by using higher tapering of field of view (FoV). We have found that diffuse Galactic synchrotron emission (DGSE) dominates the sky, after point source subtraction, across the angular multipole range $1115 \leqslant \ell \leqslant 5083$ and $1565 \leqslant \ell \leqslant 4754$ for direction-dependent and -independent calibrated visibilities, respectively. The statistical fluctuations in DGSE has been quantified as a power law of the form $\mathcal{C}_\ell = A\ell^{-\beta}$. The best-fitting values of (A, β) are $(62 \pm 6 \text{ mK}^2, 2.55 \pm 0.3)$ and $(48 \pm 4 \text{ mK}^2, 2.28 \pm 0.4)$ for the two different calibration approaches. For both the cases, the power-law index is consistent with the previous measurements of DGSE in other parts of sky.

Key words: methods: data analysis – diffuse radiation.

1 INTRODUCTION

Observations of the redshifted 21 cm 'spin-flip' transition (Field 1958) of the neutral hydrogen (H I) is considered as a promising probe for physical conditions in the early Universe (Furlanetto, Oh & Briggs 2006; Morales & Wyithe 2010, for review). Observations of Gunn–Peterson trough in quasar absorption spectra (Fan et al. 2002; Fan, Carilli & Keating 2006; Mortlock et al. 2011) and Thompson optical depth as measured from CMB temperature and polarization angular spectra (Planck Collaboration I 2018) together imply that Universe was reionized (epoch of reionization) over a

redshift range ($6 < z < 15$). Studying the early Universe through the redshifted 21 cm signal will be the first hint to understand the nature of the first stars, galaxies, and black holes and the evolution of large-scale structures in the Universe (Madau 1997; Bharadwaj, Nath & Sethi 2001a; Fan et al. 2006). The measurement of H I 21 cm power spectrum along with tomographic imaging of the IGM using large interferometric arrays holds the greatest potential to observe the redshifted H I 21 cm line (Bharadwaj & Sethi 2001; Morales & Hewitt 2004; Zaldarriaga, Furlanetto & Hernquist 2004; Bharadwaj & Ali 2005). Several upcoming and ongoing projects such as Donald C. Backer Precision Array to Probe the Epoch of Reionization (PAPER; Parsons et al. 2010; Kerrigan et al. 2018), the Low Frequency Array (LOFAR; van Haarlem et al. 2013), the Murchison Wide-field Array (MWA; Li et al. 2018), the Square

⋆ E-mail: phd1601121009@iiti.ac.in

Kilometer Array (SKA1 LOW; Koopmans et al. 2015); and the Hydrogen Epoch of Reionization Array (HERA; DeBoer et al. 2017) will have needed sensitivity to measure redshifted H I 21 cm power spectrum. However, we may need the complete SKA to do a successful tomographic imaging of IGM.

In addition, statistical detection of intensity fluctuations in post-reionization 21 cm signal ($z \lesssim 6$ or $\nu \gtrsim 200$ MHz), using intensity mapping experiment, provides a unique tool for precision cosmology. Mapping of 21 cm intensity fluctuations in post-reionization era can quantify the large-scale H I power spectrum, source clustering, etc. (Bharadwaj et al. 2001a; Bharadwaj & Pandey 2003; Bharadwaj & Ali 2005; Wyithe & Loeb 2008). BAOBAB (Pober et al. 2013a), BINGO (Battye et al. 2012), CHIME (Bandura et al. 2014), the Tianlai project (Chen et al. 2016), HIRAX (Newburgh et al. 2016), SKA1-MID (Bull et al. 2015) will measure Baryon Acoustic Oscillations (BAO) over a redshift range $z \sim 0.5 - 2.5$, which can be used as a standard ruler to constrain Dark Energy equation of state. Efforts are also ongoing to make a $\sim 5\sigma$ detection of amplitude of power spectrum $A_{H I}$ around $z \sim 3.35$ using OWFA (Subrahmanya, Manoharan & Chengalur 2017).

The expected brightness temperature of redshifted H I-signal from the epoch of reionization (EoR) and post-reionization epoch is many orders of magnitude fainter than the radio emissions from different Galactic and extragalactic foregrounds (Zaldarriaga et al. 2004; Bharadwaj & Ali 2005). The challenges are nearly identical for both EoR and post-reionization experiments. So the knowledge of foregrounds at post-reionization epoch can also help us to understand the intricacies involved in detection of the H I signal coming from EoR. Accuracy of extraction of the cosmological signal strongly depends on the ability to characterize and remove the foregrounds from observational data sets at the frequency of redshifted H I 21 cm line. Depending upon sensitivity we can identify individual sources and remove them from the image down to a certain flux level. But the effect of residual sources to the power spectrum could overwhelm the cosmological signal (Di Matteo et al. 2002; Datta, Bhatnagar & Carilli 2009). The foreground sources are diffuse Galactic synchrotron emission (DGSE) from our galaxy (Shaver et al. 1999), free–free emission from ionizing haloes (Oh & Mack 2003), faint radio-loud quasars (Di Matteo et al. 2002), synchrotron emission from low-redshift galaxy clusters (Di Matteo, Ciardi & Miniati 2004), etc.

Previous studies have shown that foreground spectra from astrophysical sources are generally smooth and correlated over a frequency separation of $\triangle \nu \sim 1$ MHz whereas the H I-signal decorrelates rapidly over such frequency separation (Bharadwaj & Sethi 2001; Bharadwaj & Ali 2005). This property allows us to separate the cosmological signal from the foregrounds (Ghosh et al. 2011). There are mainly three different techniques used to deal with foregrounds – foreground avoidance (Datta et al. 2010a; Datta, Bowman & Carilli 2010b; Trott, Wayth & Tingay 2012; Pober et al. 2013b), foreground suppression (Chapman et al. 2013; Choudhuri et al. 2016), and foreground removal (Datta et al. 2009; Chapman et al. 2016).

The basic concept of foreground removal technique is to model each foreground components precisely and subtract that model from the data set. Modelling bright point sources residing at the edge of FoV is difficult because the primary beam becomes asymmetric and highly time and frequency dependent at outer part of the FoV. It is possible to suppress the effects of bright sources at the edge of FoV by tapering the sky response using tapered gridded estimator (TGE; Choudhuri et al. 2014, 2016) (see Section 5).

Characterizing foregrounds to the best possible extent with low-frequency observations is essential to construct accurate model of foregrounds. Using these sensitive observations, we can also learn about properties of extragalactic point sources and DGSE, which apart from being two main foreground components are scientifically interesting in its own right. In addition, the knowledge of fluctuations in the Galactic synchrotron emission can be used to probe structures and magnetic field in interstellar medium of the Milky Way (Waelkens, Schekochihin & Enßlin 2009; Lazarian & Pogosyan 2012; Iacobelli et al. 2013).

In this paper, we have studied fluctuations in foregrounds of European Large-Area ISO Survey-North 1 (ELAIS-N1) with upgraded Giant Metrewave Radio Telescope (uGMRT) at 325 MHz. ELAIS-N1 has been previously studied at other frequencies (Garn et al. 2008; Sirothia et al. 2009; Jelić et al. 2014; Taylor & Jagannathan 2016). The field lies at high galactic latitude ($b = +44.48°$), therefore the contribution of Galactic synchrotron emission to foregrounds is relatively small for this patch of sky. This helps us to quantify extragalactic foreground sources with the main motivation to detect redshifted H I signal from post-EoR. This is going to be the first among a series of papers from the deep (25 h) observation of ELAIS-N1 field at this frequency. We will systematically study this field with final motivation to get upper limit on post-EoR signal. As a first step, here we present the detailed analysis of the GMRT Software Backend (GSB) data set (32 MHz bandwidth) and effectiveness of TGE to estimate angular power spectrum (APS) of point sources and DGSE. We have also studied the effect of different calibration techniques in estimation of power spectrum of DGSE. In forthcoming paper, we will present the detailed analysis of the GMRT Wideband Backend (GWB) data set (200 MHz bandwidth), source catalogue, differential source counts, cross-correlation between sources detected in other wavelengths, characterization of foreground with respect to full bandwidth (200 MHz), etc.

This paper is structured as follows. In Section 2, a brief summary of existing low-frequency observations for different fields are mentioned. We describe the uGMRT observations of ELAIS-N1 in Section 3. The details of RFI mitigation and direction-independent calibration and imaging are mentioned in Section 4. For direction-dependent calibration basic work methodology of SPAM is given in Section 4.3. We have applied TGE (Choudhuri et al. 2014, 2016) to both direction-independent and direction-dependent calibrated visibilities to determine the effect of different calibration techniques on estimation of APS ($\mathcal{C}_\ell$). A brief theory of TGE and results are presented in Section 5. Finally, Section 6 summarizes and concludes this work.

2 LOW-FREQUENCY RADIO UNIVERSE – PHYSICS AND OBSERVATIONS

The gyration of cosmic ray electrons in the magnetic field of our Galaxy is the main source of synchrotron radiation. The energy spectrum and density of cosmic ray electrons and also the magnetic field strength vary across the Galaxy. Therefore, observed synchrotron radiation will depend on frequency of observation as well as on the patch of sky we are observing through radio interferometer. Radio observations at $\nu \leq 1.4$ GHz provide the clearest picture of the Galactic synchrotron morphology, since at these frequencies the diffuse non-thermal radiation clearly dominates over all other emissions outside the Galactic plane. There are several observations covering different regions of sky spanning a wide range of frequencies to characterize DGSE. There is an all-sky map of Galactic synchrotron radiation by Haslam et al. (1982) at

Table 1. Observation summary for GWB and GSB.

	GWB	GSB
Working antennas	28	28
Central frequency	400 MHz	325 MHz
Bandwidth	200 MHz	32MHz
Visibility integration time	2 s	8 s
Number of channels	8192	512
Total observation time	25 h	25 h
Frequency resolution	24 kHz	65 kHz

Table 2. Detail of calibrators of this observation.

Flux calibrator	
Source	3C286
Flux density	23 Jy
Source	3C48
Flux density	42Jy
Scale	Scaife–Heald
Phase calibrator	
Source	J1549+506
Flux density	0.3 Jy
Target field	
Source	ELAIS N1
Time	14 h

408 MHz. A map of DGSE at 1420 MHz have presented by Reich (1982) and Reich & Reich (1988). Giardino et al. (2001) have shown using Rhodes survey at 2.3 GHz that APS ($\mathcal{C}_\ell$) of DGSE behaves like a power law,

$$\mathcal{C}_\ell = A \times (1000/\ell)^\beta, \tag{1}$$

where the power-law index $\beta = 2.43$ in the ℓ range $2 \leqslant \ell \leqslant 100$. Giardino et al. (2002) have found $\beta = 2.37$ in the ℓ range $40 \leqslant \ell \leqslant 250$ for the Parkes survey at 2.4 GHz. Bernardi et al. (2009) have analysed 150 MHz WSRT observation to characterize the fluctuations in DGSE and found that $A = 253$ mK^2 and $\beta = 2.2$ for $\ell \leqslant 900$. Ghosh et al. (2012) have reported $A = 513$ mK^2 and $\beta = 2.34$ in the ℓ range $253 \leqslant \ell \leqslant 800$ using 150 MHz GMRT observations. Iacobelli et al. (2013) have reported using LOFAR observation at 160 MHZ that fluctuations in DGSE ($\mathcal{C}_\ell$) approximately follows a power law with a slope $\beta \approx 1.8$ up to $\ell = 1300$.

Ali, Bharadwaj & Chengalur (2008) have studied the foregrounds on sub-degree angular scales with GMRT observation at 150 MHz. They have used the correlations among measured visibilities to directly determine the multifrequency APS $\mathcal{C}_\ell (\triangle\nu)$ (Datta, Choudhury & Bharadwaj 2007). They have found that the measured $\mathcal{C}_\ell (\triangle\nu)$ before point source subtraction has a value around 10^4 mK^2. This is seven orders of magnitude stronger than the expected redshifted H I signal.

La Porta et al. (2008) have calculated that APS of DGSE as a function of Galactic latitudes by considering various cuts in the sky. They have found that APS is best fitted with a power law and the power-law index lies between [2.6 and 3] for different Galactic latitudes.

Choudhuri et al. (2017) have analysed two different fields of TIFR GMRT Sky Survey at 150 MHz near the Galactic plane (9°, +10°) and (15°, −11°) to characterize the statistical properties of DGSE . They have found that the measured total intensity of APS shows a power-law behaviour in the ℓ range $240 \leqslant \ell \leqslant 580$ and $240 \leqslant \ell \leqslant 440$ and the best-fitting values of (A, β) are (356, 2.8) and (54, 2.2) for two different fields, respectively.

The outcome of all these analysis is that APS of synchrotron radiation over large portion of the sky can be modelled as a power law of the form $\mathcal{C}_\ell = A(1000/\ell)^\beta$ with $\beta \sim [1.5, 3.0]$ for $\ell \leq 1300$, corresponding to an angular scale $\theta \geq 0.2°$. This general result does not include the complexity of the APS of synchrotron emission whose parameters are expected to change with frequency and sky direction.

3 UGMRT OBSERVATION

The GMRT (Swarup et al. 1991) is one of the largest and most sensitive fully operational low-frequency radio telescopes in the world today. The array configuration of 30 antennas (each of 45 m

diameter) spanning over 25 km provides a total collecting area of about 30 000 m^2 at metre wavelengths, with a fairly good angular resolution (∼arcsec). Out of the 30 antennas, 14 antennas are randomly distributed in a Central square which is approximately 1.1 km × 1.1 km in extent. The rest of the antennas lie along three nearly 14 km long arms in an approximately 'Y' shaped configuration. Recently GMRT has been upgraded to uGMRT with some extra features, such as: (i) huge frequency coverage, from 120 to 1500 MHz; (ii) maximum bandwidth available is 400 MHz instead of 32 MHz bandwidth of original GMRT design; (iii) digital backend correlator catering to 400 MHz bandwidth; (iv) improved receiver systems with higher G/T_{sys} and better dynamic range (Gupta et al. 2017).

We carried out deep observation of the ELAIS-N1 field ($\alpha_{2000} = 16^h10^m1^s$, $\delta_{2000} = 54°30'36''$) with the uGMRT in GTAC (GMRT Time Allocation Committee) cycle 32 during May 2017 for 25 h over 4 d. The ELAIS-N1 field lies at high Galactic latitudes ($\ell = 86.95°$, $b = +44.48°$) and was up at night time during the GTAC cycle 32 and the field contains relatively few bright sources. The observation was carried out at night for all days to minimize the radio frequency interference (RFI) from manmade sources. Further the ionosphere is considerably more stable at night. We have conducted the observation for long time (25 h) to achieve high dynamic range and to get adequately sampled visibilities for further statistical analysis. For each observing session, we have observed a flux calibrator 3C286 in the beginning and 3C48 at the end of the observation run. We have observed a phase calibrator J1549+506 (near the target field) in every 25 min to correct for the temporal variations in the system gain.

The observation summary along with details of the calibrators are presented in Tables 1 and 2. The observational setup was a total 512 frequency channels spanning 32 MHz bandwidth centred at 325 MHz using GSB. The time and frequency resolution of the observation are 8 s and 65 KHz, respectively.

4 DATA ANALYSIS

4.1 RFI mitigation

RFI limits the sensitivity of radio observations by increasing the system noise and corrupting the calibration solutions. It also restricts the available frequency bandwidth. The effect is particularly strong at frequencies below 600 MHz at GMRT.

There is ringing across frequency channels that neighbour the strong, usually narrow, RFI. This phenomenon usually known as Gibbs ringing. To mitigate this ringing we have employed Hanning-

Table 3. Imaging summary.

	Direction independent (CASA)	Direction dependent (SPAM)
Image size	4096×4096	3582×3582
pixel size	$2.0\,\mathrm{arcsec} \times 2.0\,\mathrm{arcsec}$	$2.0\,\mathrm{arcsec} \times 2.0\,\mathrm{arcsec}$
Number of wprojection planes	256	256
Off-source noise	$80\,\mu\mathrm{Jy\,beam}^{-1}$	$40\,\mu\mathrm{Jy\,beam}^{-1}$
Dynamic range (peak/noise)	4000	10000
Flux density (max, min)	$(350\,\mu\mathrm{Jy}, -12\,\mathrm{mJy})$	$(390\,\mathrm{mJy}, -6\,\mathrm{mJy})$
Synthesized beam	$11\,\mathrm{arcsec} \times 6\,\mathrm{arcsec}$	$11\,\mathrm{arcsec} \times 8\,\mathrm{arcsec}$

smoothing algorithm in CASA. Hanning-smoothing applies a triangle as a smoothing kernel across the spectral axis that diminishes the ringing and also reduces the number of channels that may look bad by flagging them. As a result spectral resolution has been decreased. After that we have used an autoflag algorithm, *RFLAG*, for RFI excision. In order to get the best possible result from *RFLAG*, we have first solved for an initial set of antenna-based phases over a narrow range of channels and made an average bandpass over the entire observing session using phase calibrator. However, for final bandpass calibration we have used 3C286, which gives higher signal-to-noise ratio in the bandpass. We have applied *RFLAG* to the bandpass corrected data, where data is iterated through in segments of time and local rms and median rms of real and imaginary part of the visibilities across channels as well as across a sliding time window has been calculated. Deviation of local rms from this median value is being calculated. If local rms is larger than five times the median value of deviation, then the data was flagged. The bulk of flagging is done using *RFLAG* on all data uniformly for direction-independent and -dependent calibration. Rest is minor iterative flagging during calibration steps.

4.2 Direction-independent approach

After flagging of spurious signal present in the data set, we have done direction-independent calibration using CASA. We have calibrated individual night's data separately. The calibration is done with exactly same parameters for different night's data sets. During imaging we have used all of them to make a combined continuum image.

Calibration: We have used 3C286 as flux density and bandpass calibrator. We have used Scaife & Heald ([2012](#)) model to set the flux value of 3C286 and 3C48 using *SETJY* task in CASA. Using CASA task *BANDPASS*, we have first done bandpass calibration to account for gain variation as a function of frequency for 3C286. Then we have calculated gain and phase variations as a function of time on a 16 s time-scale, using *GAINCAL*, for all the calibrators, i.e. for flux calibrator (3C286), phase calibrator (J1549+506) and for our last scan of the calibrator 3C48. While we know the flux density of our primary calibrator (3C286), the model assumed for the secondary calibrator (J1549+506) was a point source of 1 Jy located at the phase centre. We have used the 3C286 to determine the system response to a source of known flux density and used this to find out the true flux density of J1549+506.

We have applied flux density, bandpass, gain, and phase calibration solutions from phase calibrator (J1549+506) to the target field ELIAS-N1, since it is near to the target field. During calibration bad data were flagged in various stages. In antenna based solution, data for an antenna with large error was flagged. Some baselines were also flagged based on closure error. After calibration and RFI mitigation nearly 30 per cent of on source data were flagged.

Imaging and self-calibration: The field of view ($1.4° \times 1.4°$) is large for GMRT at 325 MHz. We have taken 256 w-projection planes in the CASA task CLEAN with gridmode='widefield' to take into account the non-coplanar nature of the GMRT antenna distribution. We have used Briggs robust parameter -1 as this shifts slightly towards uniform weighting. This produces nearly Gaussian central PSF while suppressing the broad wings and suppresses the abundance of short baselines in GMRT observation. We have used multiscale multifrequency (MS-MFS) deconvolution algorithm (Rau & Cornwell [2011](#)) in CASA with nterms=2 to account for the total intensity (Stokes I) as well as the spectral term. Table [3](#) contains a summary of the imaging details with all the relevant parameters which are mostly self-explanatory.

We have carried out several rounds of self-calibration to reduce the error from temporal variations in the system gain and spatial and temporal variations in the ionospheric properties. For individual night's data, we have done phase only self-calibration on the target field for four rounds with gain-solutions 5, 4, 2, and again 2 min, respectively . The final continuum image is shown in the Fig. [1](#). We have created a large image of size $2.3° \times 2.3°$ to include the bright sources at the edge of the FoV. Otherwise, side lobes of those sources will cause ripple along frequency direction and distort the image. Here, we present only the central zoomed-in part of the image of size $1.2° \times 1.2°$. The off-source rms of the image is 80 μJy and size of the synthesized beam is 11 arcsec $\times$ 6 arcsec. Note that there are localized imaging artefacts around bright sources due to residual phase errors which have not been corrected during self-calibration.

4.3 Direction-dependent approach

For direction-dependent calibration we have used a fully automated AIPS (Greisen [1998](#)) based pipeline, Source peeling and atmospheric modelling (SPAM) (Intema et al. [2009](#), ; Intema [2014a](#),[b](#)). SPAM includes direction-dependent calibration, modelling and imaging for correcting mainly ionospheric dispersive delay. The pipeline uses ParselTongue interface (Kettenis et al. [2006](#)) to access AIPS task, files and tables from PYTHON. SPAM consists of two parts: a pre-processing part that converts raw data from individual observing session (LTA format) into pre-calibrated visibility data sets and a main pipeline part which converts pre-calibrated visibility data into stokes I continuum image.

Pre-calibration: In the pre-processing part, SPAM computes good-quality instrumental calibration from the best available scan of one of the primary calibrators and apply these calibration to the data. The data for each day has been calibrated separately. Flux density of calibrators has been set following low-frequency flux models Scaife & Heald ([2012](#)). For each scan on each calibrator after initial flagging of RFI it determined time variable complex gain solution and time constant bandpass solution per antenna and per polarization. To reduce the data size and speed up the processing,
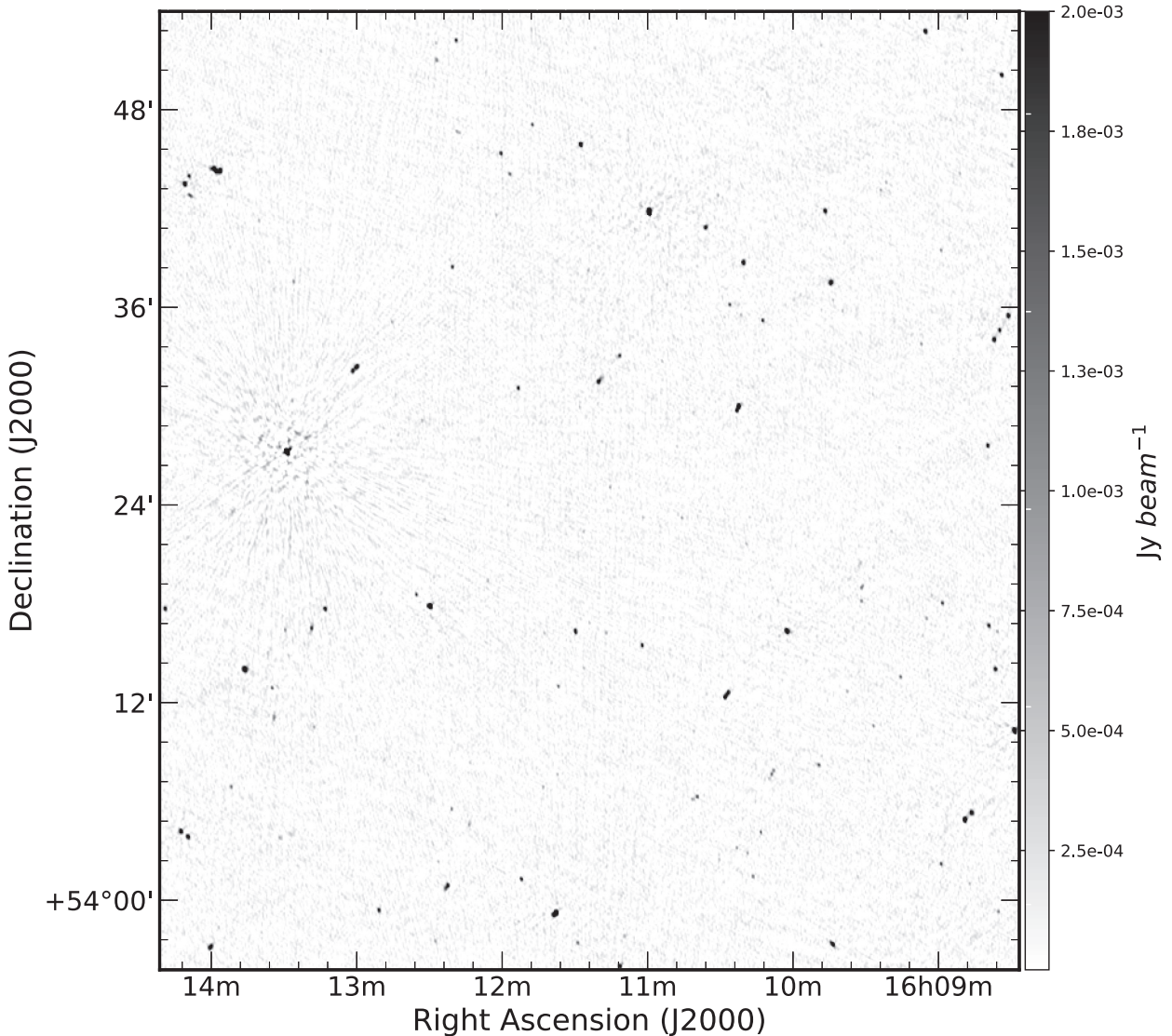
Figure 1. The above uGMRT image is total intensity map of ELIAS N1 at 325 MHz (bandwidth 32 MHz) after analysing the data with CASA where only direction independent calibration has been performed. The rms achieved is 80 μJy and beam size is 11 arcsec × 6 arcsec and the dynamic range is ∼4000.

LL and RR polarizations were combined as Stokes *I* and data was averaged in frequency and time. The final number of channels after averaging is 42 of width 0.761 MHz yielding an effective bandwidth of 32 MHz. The pipeline computes a weight factor, which is proportional to number of active antennas and inverse variance of the gain amplitude and the best calibrator scan is with the highest weight. It used best scan of 3C286 and applied the calibration solution of this calibrator to the target data. After calibration, the UV-data from all 4 d were combined.

Calibration and imaging: The main pipeline also consists two parts: a direction-independent self-calibration part and direction-dependent ionospheric calibration part. Phase-only self-calibration of the target field was started using multipoint source model of the local sky derived from the NVSS catalogue. Self-calibration was followed by wide-field imaging and CLEAN deconvolution of the primary beam area and out to five primary beam radii to include bright outliers sources to avoid negative side-lobes of those sources during imaging. It used Briggs weighting with robust parameter −1, which generally gives well-behaved point spread function (without

broad wings) by down weighting the very dense central *uv*-coverage of the GMRT. Phase-only self-calibration were repeated for three more times followed by one round of amplitude and phase self-calibration where gain solutions were determined on a longer time-scale than the phase-only solutions. Phase solutions are filtered to separate ionospheric from instrumental effects and instrumental effects were removed from visibilities (see Intema et al. 2009). Between imaging and calibration it constructed residual visibilities by first subtracting model from data and then Fourier transforming it back to visibility domain. Then any ripple artefacts in image plane will show up as a localized and high-amplitude peaks in the UV-plane and removed those from the data (Intema 2014a,b; Intema et al.)

Significant artefacts still remained near bright sources mainly because of residual phase errors due to ionosphere. The gain phases and sky model result from the direction-independent part of the pipeline were sufficient to start direction-dependent (from hereon DD) calibration. DD gain phases were obtained by peeling bright in-beam sources in the FoV yielding measures of ionospheric phase
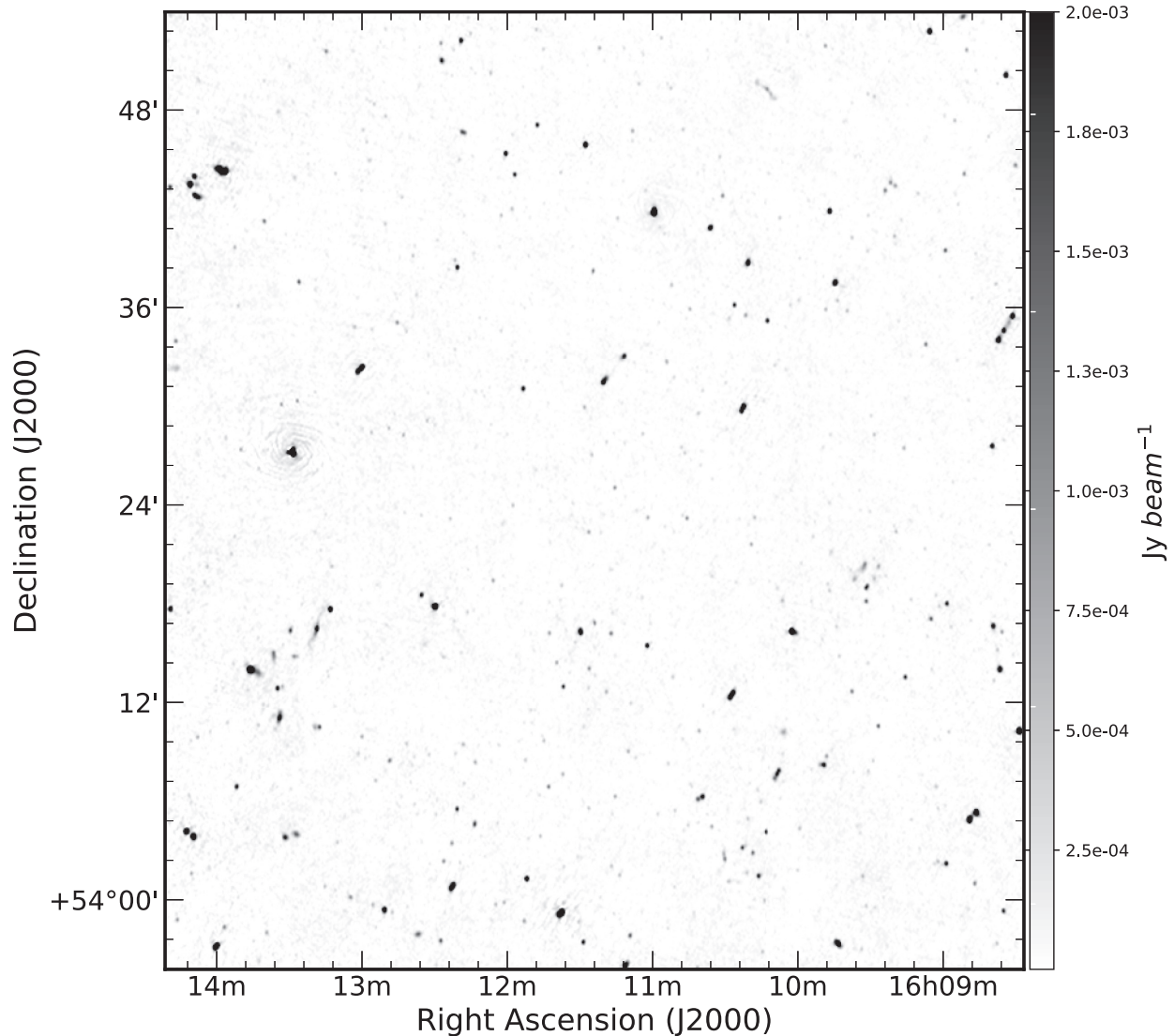
Figure 2. The uGMRT 325 MHz total intensity image of ELAIS N1 after direction-dependent calibration has been performed with SPAM. The rms noise achieved is 40 μJy and synthesized beam is 11 arcsec × 8 arcsec and the dynamic range is ~10 000.

delay. DD gain phases per time stamp were fitted with a two-layer phase screen model. During imaging of the full FoV, this model was used to calculate the phase correction per facet while applying the DD gain tables on fly. At the end of the pipeline, we got the primary beam corrected map of the target field (ELAIS-N1). The final map is shown in Fig. 2. The off-source rms of the map near the phase centre is 40 μJy beam^{-1} and beam size is 11 arcsec × 8 arcsec.

4.4 Comparison between two calibration approaches

As seen in Fig. 2, there is significant improvement in dynamic range and there are less artefacts around bright sources. Although to visualize the improvements after DD calibration, we have shown four specific sources in ELAIS-N1 field with increasing distance from the phase centre in Fig. 3. The left-hand and right-hand columns in Fig. 3 are for direction-independent and -dependent calibration, respectively, and from top to bottom source position with respect to phase centre is in increasing order. It can be seen that the reconstruction of the farthest source from phase centre (last

row of Fig. 3) is very poor in direction-independent calibration in comparison with direction-dependent one. This justifies that for wide FoV and at low-frequency observation direction-dependent calibration is required to reconstruct the sources which get affected due to bright artefacts.

5 FOREGROUND CHARACTERIZATION

After making the map with two different calibration approaches we proceed to quantify angular fluctuations in Galactic and extragalactic foregrounds. To do this we have used TGE. Here, we briefly discuss the basics of TGE and the novelty of this particular estimator, for more details see Choudhuri et al. (2014, 2016).

5.1 Tapered gridded estimator – brief background

TGE uses correlations between gridded visibilities that gives unbiased estimate of APS. Spectral smoothness of foregrounds over redshifted H I 21 cm signal holds the promise to extract the
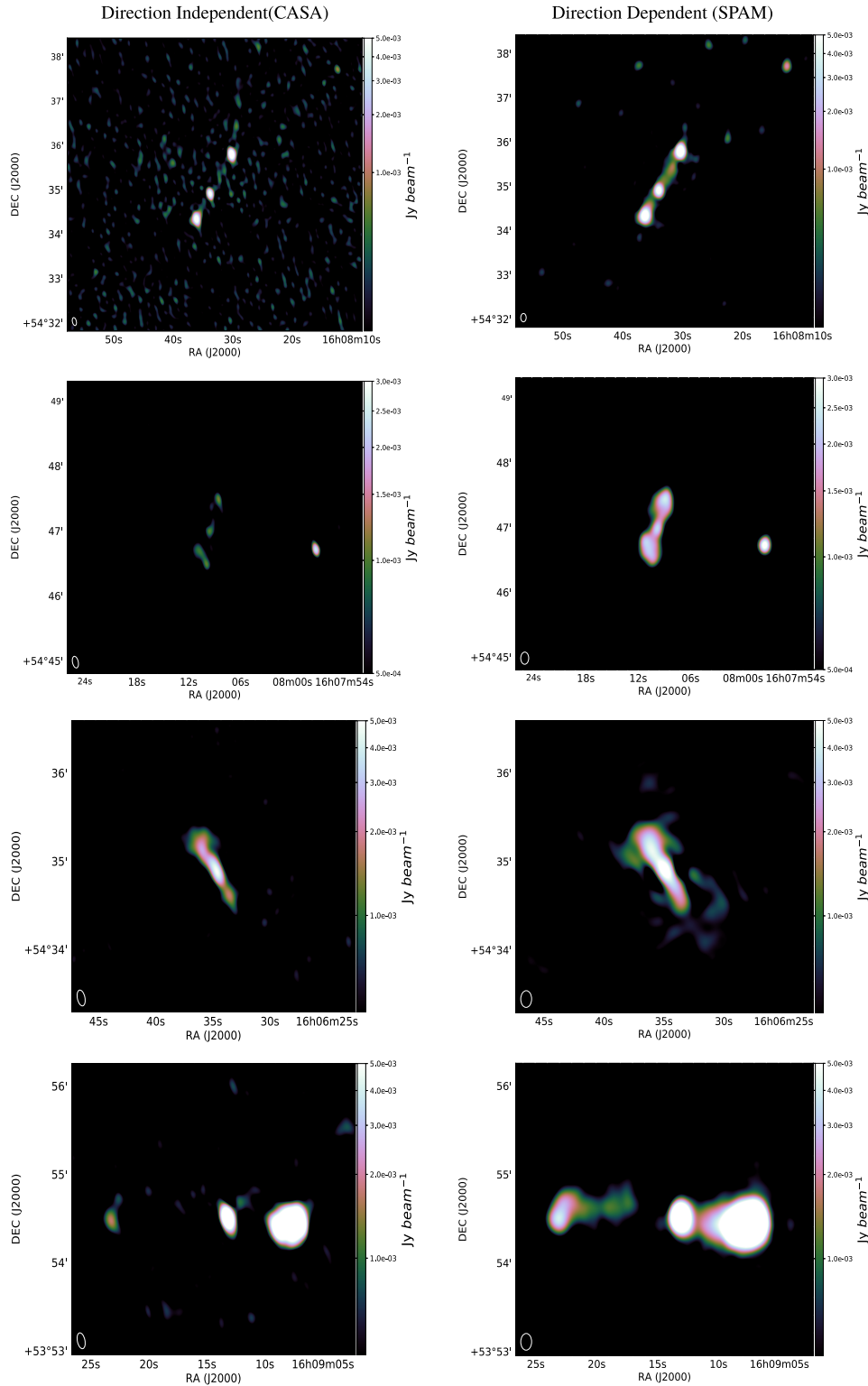
Figure 3. Left-hand and right-hand panels show some specific sources in the ELAIS-N1 field for direction-independent and -dependent calibration, respectively. The distance of sources in each row with respect to the phase centre are 0.22° (first row), 0.41° (second row), 0.53° (third row), 0.62° (fourth row).

cosmological signal amidst bright foregrounds. But bright sources at the edge of FoV can cause of oscillation in the foreground spectra and makes it un-smooth. As a result extraction of the cosmological signal becomes challenging. Side lobes of these bright sources near the nulls of the primary beam also causes difficulties to estimate

the power spectrum. TGE overcome these problems by tapering the Primary beam. It cuts off the sky response well before the first null. Another feature of TGE is it uses gridded visibilities to compute power spectrum. So it is computationally very fast. This establishes the novelty of TGE to estimate the power spectrum.

The tapering is incorporated by multiplying the sky with a Gaussian window function $\mathcal{W}(\theta) = \exp\left(\frac{-\theta^2}{\theta_w^2}\right)$, where $\theta_w < \theta_0$. As a result sky response falls off well before first null. θ_w is parametrized as $\theta_w = f\theta_0$, where f is the tapering parameter. Here, we have used $\theta_w = 44$ arcmin with $f = 1$ for direction-dependent calibrated visibilities and $\theta_w = 22$ arcmin with $f = 0.5$ for direction-independent calibrated visibilities. The reason behind this choice of tapering parameter is discussed in Section 5.3. Both of these are smaller than FWHM (72 arcmin) of the primary beam of GMRT at 325 MHz. In the visibility domain tapering is achieved by convolving the gridded visibilities in a rectangular gridded plane with the Fourier transform of $\mathcal{W}(\theta)$

$$\mathcal{V}_{cg} = \sum_i \tilde{\omega}(\boldsymbol{U_g} - \boldsymbol{U_i})\mathcal{V}_i, \tag{2}$$

where $\mathcal{V}_{cg}$ is the convolved visibilities at every grid points g, $\tilde{\omega}$ is the Fourier transform of the tapering window function $\mathcal{W}(\theta)$, and $\boldsymbol{U_g}$ refers to the baseline corresponding to the grid points. The self-correlation of the gridded and convolved visibilities can be written as

$$\langle|\mathcal{V}_{cg}|^2\rangle = \left(\frac{\partial B}{\partial T}\right)^2 \int d^2U |\tilde{K}(\boldsymbol{U_g} - \boldsymbol{U})|^2 \mathcal{C}_{2\pi U_g}$$
$$+ \sum_i |\tilde{\omega}(\boldsymbol{U_g} - \boldsymbol{U_i})|^2 \langle|\mathcal{N}_i|^2\rangle, \tag{3}$$

where

$$\tilde{K}(\boldsymbol{U_g} - \boldsymbol{U}) = \int d^2U' \tilde{\omega}(\boldsymbol{U_g} - \boldsymbol{U'})B(\boldsymbol{U'})\tilde{a}(\boldsymbol{U'} - \boldsymbol{U}) \tag{4}$$

is the 'gridding kernel' and

$$B(\boldsymbol{U}) = \sum_i \delta_D^2(\boldsymbol{U} - \boldsymbol{U_i}) \tag{5}$$

is the baseline sampling function of the measured visibilities. Under the assumption $\mathcal{C}_{2\pi U_g}$ is nearly constant across the width of $\tilde{K}(\boldsymbol{U_g} - \boldsymbol{U})$ we can approximate the convolution as

$$\langle|\mathcal{V}_{cg}|^2\rangle = \left[\left(\frac{\partial B}{\partial T}\right)^2 \int d^2U |\tilde{K}(\boldsymbol{U_g} - \boldsymbol{U})|^2\right]\mathcal{C}_{2\pi U_g}$$
$$+ \sum_i |\tilde{\omega}(\boldsymbol{U_g} - \boldsymbol{U_i})|^2 \langle|\mathcal{N}_i|^2\rangle. \tag{6}$$

Here, again the correlations of tapered gridded visibilities with itself provides an estimate of the APS.

The TGE is defined as

$$\hat{E}_g = M_g^{-1}\left(|\mathcal{V}_{cg}|^2 - \sum_i |\tilde{\omega}(\boldsymbol{U_g} - \boldsymbol{U_i})|^2 \mathcal{V}_i^2\right), \tag{7}$$

where M_g is the normalizing factor and given as

$$M_g = \left(\frac{\partial B}{\partial T}\right)^2 \int d^2U |\tilde{K}(\boldsymbol{U_g} - \boldsymbol{U})|^2 - \sum_i |\tilde{\omega}(\boldsymbol{U_g} - \boldsymbol{U_i})|^2 \mathcal{V}_0. \tag{8}$$

We have calculated M_g by using simulated visibilities corresponding to an unit APS. The second term in equation (6) gives positive noise bias, however, in equation (7) this bias is removed by subtracting the autocorrelation of visibilities. So , $\langle\hat{E}_g\rangle = \mathcal{C}_{lg}$ gives you the unbiased estimate of the APS at the angular multipole $\ell_g = 2\pi U_g$ corresponding to the baseline U_g.

5.2 Methodology and results

The map of the whole field includes mainly two astrophysical components: extragalctic point sources and Galactic diffuse emissions. We first make APS of the total data, i.e. before point source subtraction and then after subtracting those bright sources we quantify fluctuations in DGE. We have done this for both calibration approaches and compare the results. Fig. 4 shows the results of the estimated APS for direction-independent (top) and direction-dependent (bottom) calibration approaches.

Point source contribution: The red curves of both figures show the estimated $\mathcal{C}_\ell$ before point source subtraction. We have found that for both calibration processes the measured $\mathcal{C}_\ell$ is nearly 10^3 mK^2 across the entire ℓ range considered here.

We have modelled $\mathcal{C}_\ell$ using the foreground model proposed in Ali et al. (2008). The dashed line in Sky shows predicted $\mathcal{C}_\ell$ due to Poisson fluctuations of discrete point sources, where the flux density of the brightest source in the direction-independent and -dependent calibration are $S_c = 350$ mJy and $S_c = 400$ mJy, respectively. We have found that the estimated $\mathcal{C}_\ell$ before source subtraction across the entire range of angular scales probed here is nearly flat, consistent with the model prediction of Ali et al. (2008).

DGSE contribution: We model the point sources during CLEANing and subtract that model from the whole field using *UVSUB* in CASA. After source subtraction, the residual map consists of DGSE and residual point sources below the noise level. APS of DGSE is modelled, based on observations, as a power law of the form $\mathcal{C}_\ell = A\ell^{-\beta}$ and the Poisson fluctuations of residual point sources contributes as a constant term in APS (Ali et al. 2008; La Porta et al. 2008; Ghosh et al. 2012; Choudhuri et al. 2017). In Fig. 4, the Green curve shows the data points with 1σ error bars of estimated $\mathcal{C}_\ell$ after point source subtraction. There is significant drop in power for both the cases after removal of point sources. It is clear from the curve that, $\mathcal{C}_\ell$ shows two different scaling behaviour as a function of ℓ. For large angular scales (low ℓ), $\mathcal{C}_\ell$ shows decreasing pattern implying that the APS is dominated by DGSE. But beyond certain ℓ contribution of residual point sources dominates over DGSE and as a result $\mathcal{C}_\ell$ becomes flat.

The dash–dash–dotted horizontal line in orange shows the $\mathcal{C}_\ell$ predicted from the Poisson fluctuations of residual point sources below a threshold flux density of $S_c = 2.75$ mJy and $S_c = 2.50$ mJy (Fig. 4). Here, these high-flux densities (S_c) correspond to bright artefacts remaining in the residual. Except few artefacts the rest of the residual is consistent with noise.

Fitting routine: The shortest baseline for direction-independent and -dependent calibration techniques are $U = 80\lambda$ and $U = 62\lambda$ corresponding to angular scales of 42 and 55 arcmin, respectively. As a result our observation is not sensitive to intensity variation at angular scales larger than these. Considering the absence of low baselines in the visibility data and taking into account the error introduced by the approximation made during convolution in equation (6), we have excluded the ℓ range $\ell < \ell_{min} = 1500$ and 1115 for direction-independent and -dependent calibration, respectively. We have found that for the whole ℓ range beyond ℓ_{min} an analytical function of the form

$$\mathcal{C}_\ell^M = A\ell^{-\beta} + C \tag{9}$$

gives the best fit with the reduced χ^2 (χ_R^2) are 1.79 and 1.87 for direction-independent and -dependent calibration approaches, respectively. The fitted curves (in Black) are shown in Fig. 4. The best-fitting parameters are $(A, \beta, C) = (62 \pm 6, 2.55 \pm 0.30, 3.24 \pm 1.09)$ and $(48 \pm 4, 2.28 \pm 0.4, 3.02 \pm 2.01)$ for direction-independent
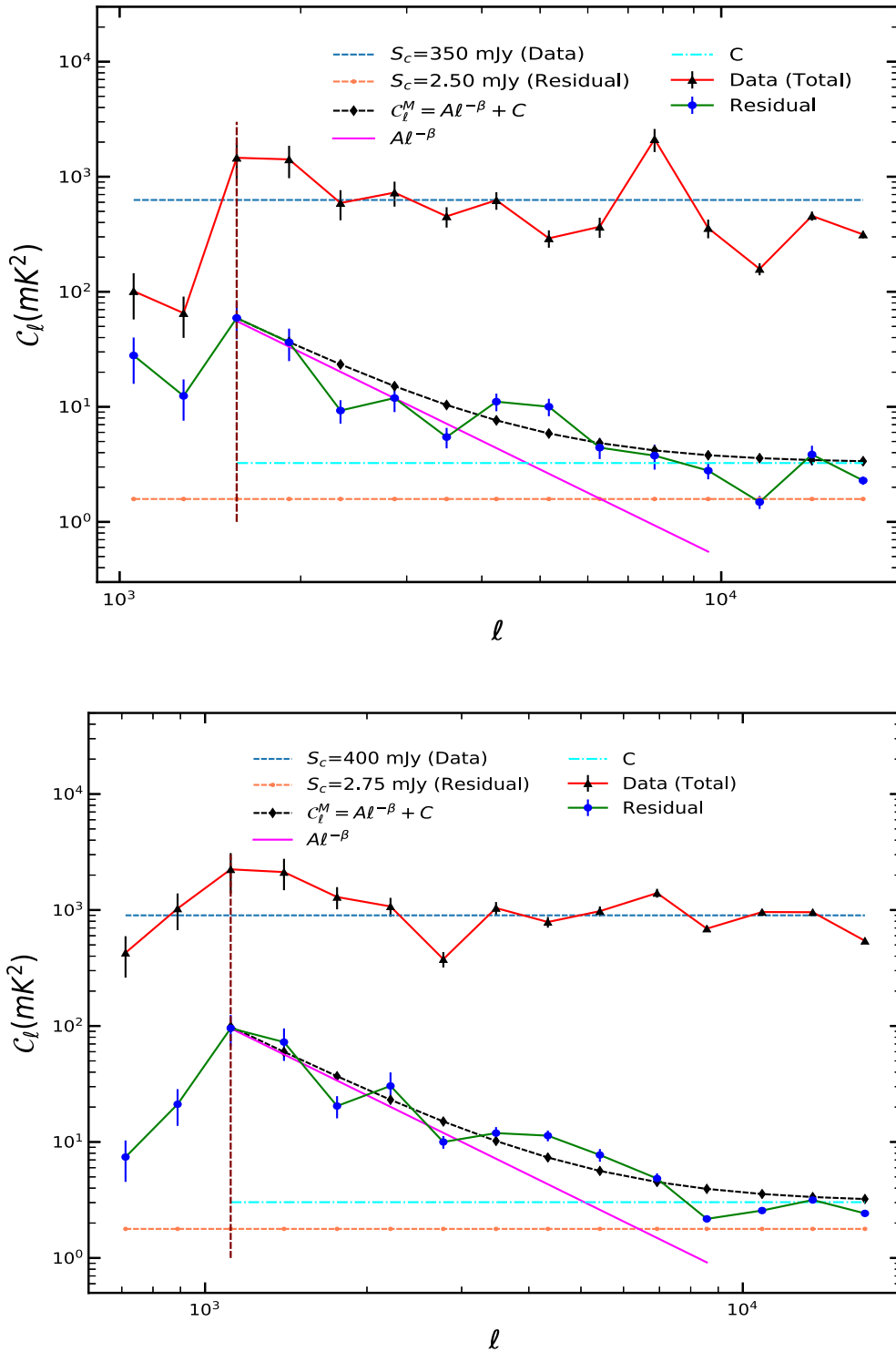
Figure 4. Estimated APS (C_ℓ) with 1σ error bars before (upper curve in Red) and after source subtraction (lower curve in Green) with tapering parameter f = 0.5 and f = 1.0 for direction-independent(top) and -dependent calibrated visibilities (bottom), respectively. The dashed line (upper horizontal line in Sky) shows foreground contribution due to discrete nature of point sources based on model prediction of Ali et al. (2008). We have excluded the points below the vertical dashed line (in Maroon) from our analysis due to convolution error. The black dashed curve shows the best-fitting model, $C_\ell^M = A(1000/\ell)^\beta + C$. The dash–dash–dotted horizontal line at the bottom shows C_ℓ predicted from the residual point sources below a threshold flux density S_c = 2.75 mJy and S_c = 2.50 mJy for direction-independent and -dependent calibration, respectively. The magenta line and the horizontal line in cyan represent the power law of the form $A(1000/\ell)^\beta$ and the constant term (C) of the best-fitting model C_ℓ^M.

Table 4. The table shows the extrapolated values of the best-fitting parameters from different observations at $\ell = 1500$ at our observing frequency for comparative study.

	Galactic coordinate (ℓ,b)	ℓ_{min}	ℓ_{max}	A (mK^2)	β	χ_R^2
ELAIS-N1 (direction-independent)	(86.95°, +44.48°)	1565	4754	62 ± 6	2.55 ± 0.3	1.79
ELAIS-N1 (direction-dependent)	(86.95°, +44.48°)	1115	5083	48 ± 4	2.28 ± 0.4	1.87
Ghosh et al. (2012)	(151.8°, +13.89°)	253	800	4.16^a	2.34 ± 0.3	
Choudhuri et al. (2016) (DATA 1)	(9°, +10°)	240	580	2.4^a	2.80 ± 0.3	0.33
Choudhuri et al. (2016) (DATA 2)	(15°, −11°)	240	440	0.46^a	2.2 ± 0.4	0.15
Bernardi et al. (2009)	(137°, +8°)	100	900	2.17^a	2.2 ± 0.3	
Iacobelli et al. (2013)	(137°, +7°)	100	1300	−	1.84 ± 0.2	
	(−, ≥ + 10°)	−	−	1.05^b	2.88	
	(−, ≤ − 10°)	−	−	1.34^b	2.74	
	(−, ≥ + 20°)	−	−	0.5^b	2.88	
La Porta et al. (2008)	(−, ≤ − 20°)	−	−	0.3^b	2.83	
	(−, ≥ + 10°)	−	−	4.28^c	2.80	
	(−, ≤ − 10°)	−	−	4^c	2.70	
	(−, ≥ + 20°)	−	−	1.67^c	2.83	
	(−, ≤ − 20°)	−	−	0.64^c	2.87	

^{a}Extrapolated from 150 to 325 MHz.
^{b}Extrapolated from 1420 to 325 MHz.
^{c}Extrapolated from 408 to 325 MHz.

and -dependent calibration, respectively. For both the cases we have quoted the value of normalized amplitude at $\ell = 1500$. We have also plotted the power law of the form $\mathcal{C}_\ell = A\ell^{-\beta}$ with best-fitting values of (A, β) (in magenta) and the constant term C (in cyan). It is evident from the plots that residual sources (the flat part) become dominant over DGSE beyond the intersection point of these two lines at $\ell = 4754$ and 5083 for direction-independent and -dependent calibration techniques, respectively. So, for DGSE estimated $\mathcal{C}_\ell$ can be well modelled as a power law for ℓ range $1565 \leqslant \ell \leqslant 4754$ and $1115 \leqslant \ell \leqslant 5083$ for direction-independent and -dependent calibration approaches, respectively. This steep spectrum is characteristic of fluctuations in DGSE.

Other observations: It is well established from observations that strength of DGSE is different for different line of sight and for different frequencies. So, it is not justifiable to compare amplitude of APS obtained in different observations at different frequencies. Despite this to check consistency, we have extrapolated the amplitude of $\mathcal{C}_\ell$ obtained from different observations (La Porta et al. 2008; Bernardi et al. 2009; Ghosh et al. 2012; Choudhuri et al. 2016) at our observing frequency (325 MHz) at $\ell = 1500$ using spectral index $\alpha = -2.5$ ($\mathcal{C}_\ell \propto \nu^{2\alpha}$). The extrapolated values of amplitude together with angular spectral index (β) are mentioned in Table 4. For all cases, the best-fitting parameter β lies within the range of 1.5–3.0 at 150 MHz and higher frequencies.

5.3 Robustness of the TGE for direction-dependent effects

We have already mentioned in Section 5 that novelty of TGE is it tapers the sky response well before first null of the primary beam. The tapering is quantified by the parameter f. Decreasing the value of f gives higher tapering of primary beam. As a result the effect of bright point sources at the outer region of FoV gets reduced. So at large angular scales we expect to get a steep power-law pattern in estimated $\mathcal{C}_\ell$. Choudhuri et al. (2016) has shown with simulated visibility data for GMRT that with increasing tapering of FoV the fractional deviation of estimated power spectrum from model power spectrum (input of simulation) gets reduced. In other words, this implies that higher tapering gives better result for recovering of input model of APS.

To validate this we have applied TGE with different tapering parameters (f) and the results are presented in Fig. 5. We have shown the estimated $\mathcal{C}_\ell$ with $f = 0.5$ and $f = 1.0$ for both calibration processes and only the power-law fitted line (in magenta) for clarity. We have found that for direction-dependent calibration, different tapering gives nearly same results. For both tapering parameters, we have found a range of ℓ where estimated $\mathcal{C}_\ell$ behaves like a power law and the fitted parameters are also same within 2σ ($A = 67 \pm 8$, $\beta = 3.0 \pm 0.4$, for $f = 0.5$ and $A = 48 \pm 4$, $\beta = 2.28 \pm 0.39$, for $f = 1.0$).

In case of direction-independent calibration, we have found some random fluctuations at certain ℓ, for less tapering of sky response with $f = 1.0$. These fluctuations mainly occur due to bright artefacts at some localized regions. Increased tapering ($f = 0.5$) however reduced the FoV and suppressed the effect of those bright sources and we got a power-law pattern in estimated $\mathcal{C}_\ell$. Phase only self-calibration failed to suppress the effect of bright artefacts at large angular distances for direction-independent calibration. So, we need higher tapering of sky response to suppress those effects in estimating APS. Whereas direction-dependent calibration minimized the effect of bright sources at large angular scales. So, reducing sky response with different f parameter does not have any significant effect in estimation of $\mathcal{C}_\ell$. This effectively validates robustness of TGE for unbiased estimation of APS from visibility data.

But due to higher tapering we are unable to recover $\mathcal{C}_\ell$ for low ℓ (≤ 1565) values in direction-independent calibration approach. Whereas for direction-dependent calibration we have measured $\mathcal{C}_\ell$ up to $\ell = 1115$. In other words, we have information for large angular scales for direction-dependent calibration technique due to less tapering of FoV.

6 DISCUSSION

We have observed the ELAIS-N1 field with uGMRT at 325 MHz with main motivation to characterize foregrounds in this field. We have calibrated the visibility data with and without direction-dependent calibration techniques and made two separate continuum images. There is significant improvement in dynamic range after direction-dependent ionospheric calibration has been performed
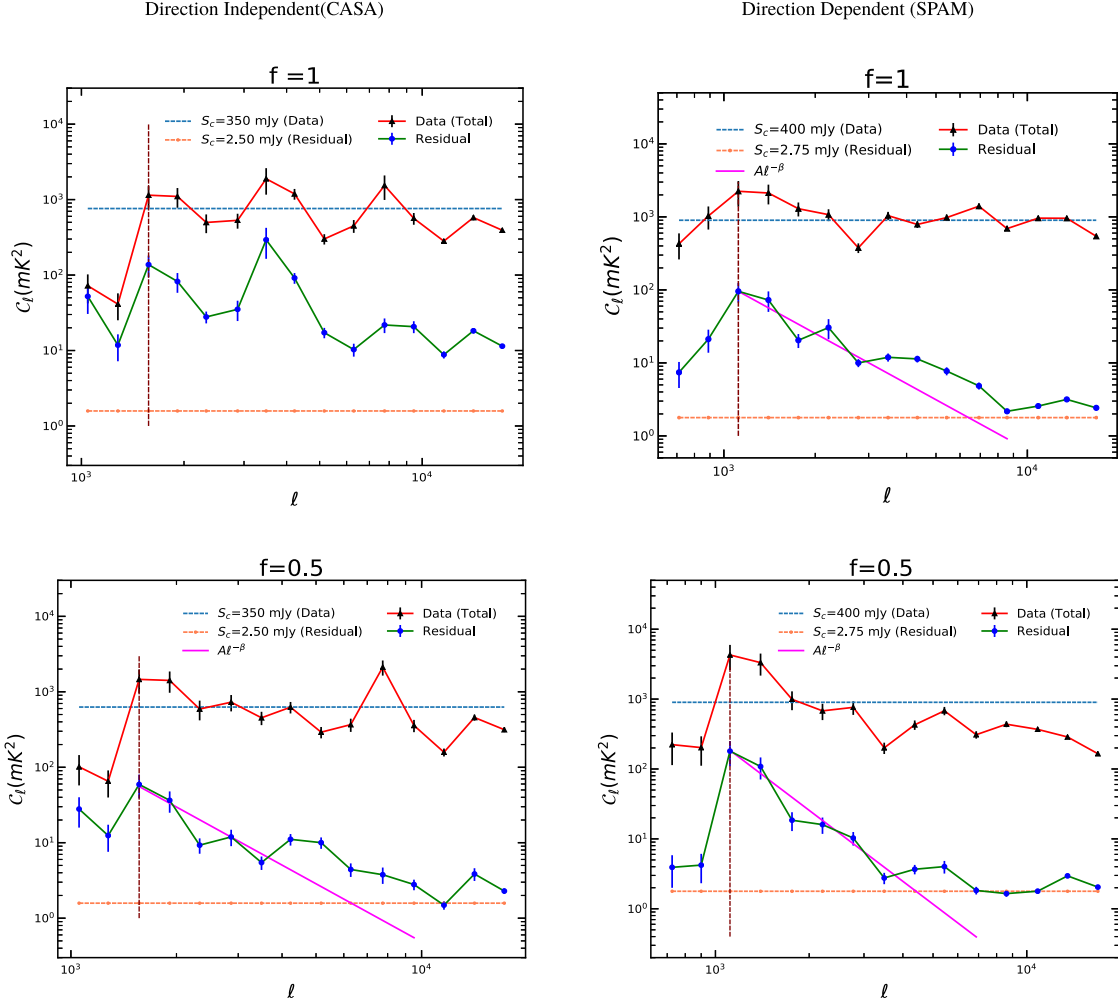
Direction Independent(CASA)   Direction Dependent (SPAM)

Figure 5. Here, we have plotted power spectrum with different tapering parameter (*f*). The left-hand column shows the estimated power spectrum for direction-independent calibration and right-hand column is for direction-dependent calibration with different tapering parameters $f = 1.0$ (top row) and $f = 0.5$ (bottom row).

and also the imaging artefacts around bright sources have been minimized. We have estimated the APS for both direction-independent and -dependent calibrated visibility data sets using TGE. We have found that before source subtraction at most of the ℓ scales probed here estimated $\mathcal{C}_\ell$ is nearly 10^3 mK^2 and remain flat except at lower ℓ where deconvolution error is significant. We can conclude that the measured $\mathcal{C}_\ell$ is point source dominated and is more than five to six orders of magnitude higher than the expected H I signal.

After subtraction of point sources from the entire FoV, the estimated $\mathcal{C}_\ell$ for residual in both cases have shown a steep power-law behaviour at low ℓ range, which is characteristics of DGSE. We have found a power-law fit for a specific ℓ range and the best-fitting amplitude and power-law index are $(A, \beta) = (62, 2.55)$ and $(48, 2.28)$ for direction-independent and -dependent calibrations, respectively. The slope of APS is consistent with the measurements of the previous observations at low frequencies.

We have also estimated the power spectrum using different tapering parameters (*f*). We have shown that higher tapering of sky response is required to get rid of undesired effects of bright sources in estimating $\mathcal{C}_\ell$ for direction-independent calibration in comparison with direction-dependent one. This validates the robustness of TGE with real data. This fact is well established in Choudhuri et al. (2016) for simulated visibility data for GMRT.

Analytic estimates of the H I signal shows that at low frequencies the amplitude of H I signal is nearly 10^{-1} mK^2, which is very feeble in comparison with bright foregrounds. After point source subtraction the estimated $\mathcal{C}_\ell$ for DGSE is still two to three orders of magnitude higher than the expected H I signal. Proper modelling of point sources and perfect subtraction from the data is very crucial to extract this faint H I signal. But as foreground spectrum is smooth in comparison to H I signal, it does not decorrelate faster than the H I signal with frequency. This fact is the key to extract the faint H I signal from strong foregrounds.

The measured $\mathcal{C}_\ell$ for DGSE is different for different patch of sky and at different frequencies. We have analysed the ELAIS-N1 field to characterize the foregrounds at sub-degree angular scales. The characterization of foregrounds will help us to extract H I signal when the data will be available from upcoming experiments like HERA, PAPER, SKA-low, SKA-mid, etc. But it is evident from Table 4 that only few observations are available across different patches of sky at these low frequencies. For those, the corresponding APS for foregrounds are available in literature. In order to constrain the foreground across wide patches of the sky, there is a need to extend sensitive low-frequency observations at different patches of the sky. In our second paper, we will present the analysis for a wider bandwidth data (200 MHz). However, even

with this limited bandwidth, we have been able to constrain the foreground APS and demonstrate the efficiency of TGE against direction-dependent effects.

We also plan to extend this work for other well-known target fields at low frequency with continuum observation to find out the variation in the nature of DGSE.

ACKNOWLEDGEMENTS

REFERENCES

Ali S. S., Bharadwaj S., Chengalur J. N., 2008, MNRAS, 385, 2166
Bandura K. et al., 2014 , in Stepp L. M., Gilmozzi R., Hall H. J., eds, Proc. SPIE Conf. Ser. Vol. 9145, Ground-based and Airborne Telescopes V. SPIE, Bellingham, p. 914522
Battye R. A. et al., 2012, preprint(arXiv:1209.1041)
Bernardi G. et al., 2009, A&A, 500, 965
Bharadwaj S., Ali S. S., 2005, MNRAS, 356, 1519
Bharadwaj S., Pandey S. K., 2003, J. Astrophys. Astron., 24, 23
Bharadwaj S., Sethi S. K., 2001, J. Astrophys. Astron., 22, 293
Bharadwaj S., Nath B. B., Sethi S. K., 2001, J. Astrophys. Astron., 22, 21
Bull P., Ferreira P. G., Patel P., Santos M. G., 2015, ApJ, 803, 21
Chapman E. et al., 2013, MNRAS, 429, 165
Chapman E., Zaroubi S., Abdalla F. B., Dulwich F., Jelić V., Mort B., 2016, MNRAS, 458, 2928
Chen Z. P., Wang R. L., Peterson J., Chen X. L., Zhang J. Y., Shi H. L., 2016, Proc. SPIE Conf. Ser. Vol. 9906, Design and Analysis of a Large Cylinder Antenna Array in Tianlai. SPIE, Bellingham, p. 99065W
Choudhuri S., Bharadwaj S., Ghosh A., Ali S. S., 2014, MNRAS, 445, 4351
Choudhuri S., Bharadwaj S., Chatterjee S., Ali S. S., Roy N., Ghosh A., 2016, MNRAS, 463, 4093
Choudhuri S., Bharadwaj S., Ali S. S., Roy N., Intema H. T., Ghosh A., 2017, MNRAS, 470, L11
Datta K. K., Choudhury T. R., Bharadwaj S., 2007, MNRAS, 378, 119
Datta A., Bhatnagar S., Carilli C. L., 2009, ApJ, 703, 1851
Datta A., Carilli C. L., Bhatnagar S., Bowman J. D., 2010a , American Astronomical Society Meeting, 42, 325.02
Datta A., Bowman J. D., Carilli C. L., 2010b, ApJ, 724, 526
DeBoer D. R. et al., 2017, PASP, 129, 045001
Di Matteo T., Perna R., Abel T., Rees M. J., 2002, ApJ, 564, 576
Di Matteo T., Ciardi B., Miniati F., 2004, MNRAS, 355, 1053
Fan X., Narayanan V. K., Strauss M. A., White R. L., Becker R. H., Pentericci L., Rix H.-W., 2002, AJ, 123, 1247
Fan X., Carilli C. L., Keating B., 2006, ARA&A, 44, 415
Field G. B., 1958, Proc. IRE, 46, 240
Furlanetto S. R., Oh S. P., Briggs F. H., 2006, Phys. Rep., 433, 181
Garn T., Green D. A., Riley J. M., Alexander P., 2008, MNRAS, 383, 75
Ghosh A., Bharadwaj S., Ali S. S., Chengalur J. N., 2011, MNRAS, 411, 2426
Ghosh A., Prasad J., Bharadwaj S., Ali S. S., Chengalur J. N., 2012, MNRAS, 426, 3295

Giardino G., Banday A. J., Fosalba P., Górski K. M., Jonas J. L., O'Mullane W., Tauber J., 2001, A&A, 371, 708
Giardino G., Banday A. J., Górski K. M., Bennett K., Jonas J. L., Tauber J., 2002, A&A, 387, 82
Greisen E. W., 1998, in Albrecht R., Hook R. N., Bushouse H. A., eds, ASP Conf. Ser. Vol. 145, Astronomical Data Analysis Software and Systems VII. Astron. Soc. Pac., San Francisco, p. 204
Gupta Y. et al., 2017, Curr. Sci., 113, 707
Haslam C. G. T., Salter C. J., Stoffel H., Wilson W. E., 1982, A&AS, 47, 1
Iacobelli M. et al., 2013, A&A, 558, A72
Intema H. T., 2014a, Astrophysics Source Code Library, record ascl:1408.006
Intema H. T., 2014b, in Chengalur J. N., Gupta Y., eds, ASI Conf. Ser. Vol. 13, SPAM: A Data Reduction Recipe for High-Resolution, Low-Frequency Radio-Interferometric Observations, Bull. Astr. Soc. India
Intema H. T., van der Tol S., Cotton W. D., Cohen A. S., van Bemmel I. M., Röttgering H. J. A., 2009, A&A, 501, 1185
Jelić V. et al., 2014, A&A, 568, A101
Kerrigan J. R. et al., 2018, ApJ, 864, 131
Kettenis M., van Langevelde H. J., Reynolds C., Cotton B., 2006 , in Gabriel C., Arviset C., Ponz D., Solano E., eds, ASP Conf. Ser. Vol. 351, Astronomical Data Analysis Software and Systems XV. Astron. Soc. Pac., San Francisco, p. 497
Koopmans L. et al., 2015, aska.conf, 1
La Porta L., Burigana C., Reich W., Reich P., 2008, A&A, 479, 641
Lazarian A., Pogosyan D., 2012, ApJ, 747, 5
Li W. et al., 2018, ApJ, 863, 170
Madau P., 1997, seim.proc, 295
Morales M. F., Hewitt J., 2004, ApJ, 615, 7
Morales M. F., Wyithe J. S. B., 2010, ARA&A, 48, 127
Mortlock D. J. et al., 2011, Nature, 474, 616
Newburgh L. B. et al., 2016, in Hall H. J. , Gilmozzi R., Marshall H. K., eds, Proc. SPIE Conf. Ser. Vol. 9906, Ground-based and Airborne Telescopes VI. SPIE, Bellingham, p. 99065X
Oh S. P., Mack K. J., 2003, MNRAS, 346, 871
Parsons A. R. et al., 2010, AJ, 139, 1468
Planck Collaboration I, 2018, A&A, 596, A108
Pober J. C. et al., 2013a, AJ, 145, 65
Pober J. C. et al., 2013b, ApJ, 768, L36
Rau U., Cornwell T. J., 2011, A&A, 532, A71
Reich W., 1982, A&AS, 48, 219
Reich P., Reich W., 1988, A&AS, 74, 7
Scaife A. M. M., Heald G. H., 2012, MNRAS, 423, L30
Shaver P. A., Windhorst R. A., Madau P., de Bruyn A. G., 1999, A&A, 345, 380
Sirothia S. K., Dennefeld M., Saikia D. J., Dole H., Ricquebourg F., Roland J., 2009, MNRAS, 395, 269
Subrahmanya C. R., Manoharan P. K., Chengalur J. N., 2017, J. Astrophys. Astron., 38, 10
Swarup G., Ananthakrishnan S., Kapahi V. K., Rao A. P., Subrahmanya C. R., Kulkarni V. K., 1991, Curr. Sci., 60, 95
Taylor A. R., Jagannathan P., 2016, MNRAS, 459, L36
Trott C. M., Wayth R. B., Tingay S. J., 2012, ApJ, 757, 101
van Haarlem M. P. et al., 2013, A&A, 556, A2
Waelkens A. H., Schekochihin A. A., Enßlin T. A., 2009, MNRAS, 398, 1970
Wyithe J. S. B., Loeb A., 2008, MNRAS, 383, 606
Zaldarriaga M., Furlanetto S. R., Hernquist L., 2004, ApJ, 608, 622

This paper has been typeset from a TEX/LATEX file prepared by the author.